

E_m , the simulation suggests that this matrix becomes much closer to the ideal one (keeping almost ideal outputs for $|10\rangle$ and $|11\rangle$ input states) if we slightly decrease the rise/fall time, say by 25% (red lines in Fig. 4), or decrease E_{J2} by a similar amount.

We controlled our two-qubit solid-state circuit by applying a sequence of pulses, and demonstrated the conditional gate operation. Although in the present experiment we paid attention only to the amplitude of the quantum state, phase evolution during the gate operation should also be examined for the realization of the quantum C-NOT gate (probably with additional phase factors), which is a constituent of the universal gate. □

Received 25 June; accepted 19 August 2003; doi:10.1038/nature02015.

1. Nakamura, Y., Pashkin, Yu. A. & Tsai, J. S. Coherent control of macroscopic quantum states in a single-Cooper-pair box. *Nature* **398**, 786–788 (1999).
2. Vion, D. *et al.* Manipulating the quantum state of an electrical circuit. *Science* **296**, 886–889 (2002).
3. Yu, Y., Han, S., Chu, X., Chu, S.-I. & Wang, Z. Coherent temporal oscillations of macroscopic quantum states in a Josephson junction. *Science* **296**, 889–892 (2002).
4. Martinis, J. M., Nam, S., Aumentado, J. & Urbina, C. Rabi oscillations in a large Josephson-junction qubit. *Phys. Rev. Lett.* **89**, 117901 (2002).
5. Chiorescu, I., Nakamura, Y., Harmans, C. J. P. M. & Mooij, J. E. Coherent quantum dynamics of a superconducting flux qubit. *Science* **299**, 1869–1871 (2003).
6. Vandersypen, L. M. K. *et al.* Experimental realization of Shor's quantum factoring algorithm using nuclear magnetic resonance. *Nature* **414**, 883–887 (2001).
7. Gulde, S. *et al.* Implementation of the Deutsch-Jozsa algorithm on an ion-trap quantum computer. *Nature* **421**, 48–50 (2003).
8. Nielsen, M. A. & Chuang, I. L. *Quantum Computation and Quantum Information* (Cambridge Univ. Press, Cambridge, UK, 2000).
9. Pashkin, Yu. A. *et al.* Quantum oscillations in two coupled charge qubits. *Nature* **421**, 823–826 (2003).
10. Berkley, A. J. *et al.* Entangled macroscopic quantum states in two superconducting qubits. *Science* **300**, 1548–1550 (2003).
11. Shnirman, A., Schön, G. & Hermon, Z. Quantum manipulations of small Josephson junctions. *Phys. Rev. Lett.* **79**, 2371–2374 (1997).
12. Averin, D. V. Adiabatic quantum computation with Cooper pairs. *Solid State Commun.* **105**, 659–664 (1998).
13. Bouchiat, V., Vion, D., Joyez, P., Esteve, D. & Devoret, M. H. Quantum coherence with a single Cooper pair. *Phys. Scripta* **T76**, 165–170 (1998).
14. Pothier, H., Lafarge, P., Urbina, C., Esteve, D. & Devoret, M. H. Single-electron pump based on charging effects. *Europhys. Lett.* **17**, 249–254 (1992).
15. Fulton, T. A., Gammel, P. L., Bishop, D. J., Dunkleberger, L. N. & Dolan, G. J. Observation of combined Josephson and charging effects in small tunnel junction circuits. *Phys. Rev. Lett.* **63**, 1307–1310 (1989).
16. Nakamura, Y., Pashkin, Yu. A., Yamamoto, T. & Tsai, J. S. Charge echo in a Cooper-pair box. *Phys. Rev. Lett.* **88**, 047901 (2002).

Acknowledgements We thank B. L. Altshuler, D. V. Averin, S. Ishizaka, F. Nori, T. Tilma, C. Urbina and J. Q. You for discussions.

Competing interests statement The authors declare that they have no competing financial interests.

Correspondence and requests for materials should be addressed to T.Y. (yamamoto@frl.cl.nec.co.jp).

High-*Q* photonic nanocavity in a two-dimensional photonic crystal

Yoshihiro Akahane^{1,2}, Takashi Asano¹, Bong-Shik Song¹ & Susumu Noda¹

¹Department of Electronic Science and Engineering, Kyoto University, Katsura, Nishikyo-ku, Kyoto 615-8510, Japan

²Advanced Materials R&D Laboratories, Sumitomo Electric Industries, Ltd, Itami, Hyogo 664-0016, Japan

Photonic cavities that strongly confine light are finding applications in many areas of physics and engineering, including coherent electron-photon interactions¹, ultra-small filters^{2,3}, low-threshold lasers⁴, photonic chips⁵, nonlinear optics⁶ and quantum information processing⁷. Critical for these applications

is the realization of a cavity with both high quality factor, *Q*, and small modal volume, *V*. The ratio *Q/V* determines the strength of the various cavity interactions, and an ultra-small cavity enables large-scale integration and single-mode operation for a broad range of wavelengths. However, a high-*Q* cavity of optical wavelength size is difficult to fabricate, as radiation loss increases in inverse proportion to cavity size. With the exception of a few recent theoretical studies^{8–10}, definitive theories and experiments for creating high-*Q* nanocavities have not been extensively investigated. Here we use a silicon-based two-dimensional photonic-crystal slab to fabricate a nanocavity with *Q* = 45,000 and *V* = 7.0 × 10⁻¹⁴ cm³; the value of *Q/V* is 10–100 times larger than in previous studies^{4,11–14}. Underlying this development is the realization that light should be confined gently in order to be confined strongly. Integration with other photonic elements is straightforward, and a large free spectral range of 100 nm has been demonstrated.

The *Q* of a cavity is determined by the energy loss per cycle versus the energy stored. With no absorption by the cavity material, *Q* is determined by the reflection loss at the interface between the interior and exterior of the cavity. Total internal reflection (TIR) and/or Bragg reflection are generally used for light confinement. For a cavity with a size much larger than the wavelength of light, a very high *Q* has already been achieved^{14,15}. In that case, the behaviour of light confined in a large cavity obeys ray optics theory, and each ray of light reflected at the interface can be designed to fulfil TIR or Bragg reflection conditions. For much smaller cavities, deviation from ray optics becomes serious, and *Q* is greatly reduced. Light confined in a very small cavity consists of numerous plane wave components with wavevectors (**k**) of various magnitudes (*k*) and directions owing to the localization of light. As it is difficult to design all such plane wave components to obey TIR or Bragg reflection conditions, photonic nanocavities with very high *Q* factors have yet to be realized.

One of the best approaches to resolving the problem is the extension of the Bragg reflection effect in multiple directions. Structures having a two- or three-dimensional (2D or 3D) periodic change of refractive index on the scale of the light wavelength are required for such extension. These are known as photonic crystals, from an analogy to solid crystals^{5,16}. For a 3D photonic crystal, Bragg reflection conditions can be fulfilled for all the propagation directions of light in a certain frequency range, known as the photonic bandgap. A small disorder or defect introduced into the 3D photonic crystal would become an ultimate photonic nanocavity, with ultra-large *Q/V*. However, 3D photonic crystals with sufficiently strong optical confinement have yet to be created⁵.

A cavity surrounded by a 2D photonic crystal is considered a feasible solution. A 2D photonic-crystal slab, as shown in Fig. 1a, with a thickness of the order of the light wavelength is very promising, owing to strong optical confinement for both in-plane and vertical directions^{2,3}. The photonic-bandgap effect is used for light confinement in the in-plane direction, and TIR, at the interface between the slab and the air clad, in the vertical direction. Apparently, fulfilment of the TIR condition in the vertical direction is crucial in designing high-*Q/V* cavities.

To investigate vertical confinement in 2D photonic-crystal slabs, we first consider a simplified model (Fig. 2a), where the cavity consists of a dielectric material with thickness *T* and length *L*. Both sides of the cavity are closed by perfect mirrors, confining light in the *x* direction. The structure is assumed to be uniform in the *y* direction for simplicity. Light is confined by TIR in the *z* direction by the air clad, as discussed above. Figure 2b shows an example of the electric field profile inside a cavity with a very short length, 2.5λ, where λ is the resonant wavelength of light in the cavity.

The strength of the vertical (*z*-direction) confinement by TIR can be investigated by decomposing the electric field inside a cavity into a set of plane wave components with various **k**-vectors by spatial

Fourier transformation (FT), which is a similar approach to that reported in ref. 10. When the tangential component of the k -vector ($|k_{\parallel}|$ or $|k_x|$) of each plane wave lies within the range 0 to $2\pi/\lambda_0$ (where λ_0 is the wavelength of light in air), the wave can escape from the cavity to the air clad, because the conservation law for $|k_{\parallel}|$ (or Snell's law in the broad sense) is satisfied at the interface between the cavity and air clad, which leads to weak vertical confinement. Note that $|k_{\parallel}|$ in the air clad can take a value from 0 to $2\pi/\lambda_0$ depending on the propagation direction in the x - z plane, while $|k_{\parallel}|$ in the cavity takes a variety of values owing to the localization of light, as explained before. When $|k_{\parallel}|$ in the cavity is larger than $2\pi/\lambda_0$, the $|k_{\parallel}|$ conservation law does not hold at the interface, and light becomes strongly confined inside the cavity, which leads to strong vertical confinement. Figure 2c shows the spatial FT spectra of the electric field of Fig. 2b, where the leaky region ($|k_{\parallel}|$ is smaller than $2\pi/\lambda_0$) is indicated. Large components exist inside the leaky region, which indicates that large radiation loss occurs in the cavity.

We now consider the loss mechanism in more detail. The electric field profile inside the cavity can be expressed as a product of a fundamental sinusoidal wave with wavelength λ , and an envelope function $F(x)$ that is determined by the cavity structure. The fundamental wave gives a delta functional FT spectrum with peaks at $k = \pm 2\pi/\lambda$, while the envelope function modifies the spectrum. In the case of Fig. 2b, the envelope function is $F(x) = 1$ (for $x = -L/2$ to $L/2$) and $F(x) = 0$ (for all other x), and the corresponding FT spectrum is a sinc function with a width of about $2\pi/L$ (Fig. 2c). Although the peak of the spectrum originating from the fundamental wave is outside the leaky region, an abrupt change in the envelope function at the edges ($x = -L/2, L/2$) generates large components inside the leaky region, leading to large radiation loss. The smaller the cavity, the more serious the edge effect, drastically decreasing the Q factor.

This gives an important hint for suppressing radiation loss: the spatial variation of the envelope function at the cavity edges should not be abrupt but gentle, so that the FT spectrum does not have components inside the leaky region. On the basis of this idea, we

have used a gaussian function for $F(x)$, as shown schematically in Fig. 2d; the calculated FT spectrum is shown in Fig. 2e. The situation has drastically changed: there are very small components inside the leaky region, when compared with Fig. 2c. This suggests that the Q factor can be increased significantly by tailoring the envelope function while keeping the mode volume small.

A physical design of a high- Q photonic nanocavity has thus been carried out using a 2D photonic-crystal slab (Fig. 1b and c). The base structure is composed of Si with a triangular lattice of air 'rods' with lattice constant a ($= 0.42 \mu\text{m}$). The thickness of the slab and the radii of the air rods are $0.6a$ ($0.25 \mu\text{m}$) and $0.29a$ ($0.12 \mu\text{m}$), respectively. We made the initial structure of the cavity with three missing air rods in a line¹⁷ (Fig. 1b). With this structure, light can be confined by Bragg reflection for the in-plane directions. For the z direction, light is confined by the air clad.

The electric field profile (E_y) of the fundamental mode of the cavity at the centre plane of the slab is shown in Fig. 3a. We used 3D finite-difference time-domain methods for the calculation. Unlike the model discussed in Fig. 2, x - and y -directional (2D) FT spectra are necessary for the investigation of the vertical confinement, as light is confined two-dimensionally in the cavity. For the same reason, the TIR condition (or k_{\parallel} conservation law) should be expanded two-dimensionally. Considering in-plane 2D propagation, the TIR condition is broken for plane waves having k_{\parallel} inside a circle of diameter $2\pi/\lambda_0$.

Figure 3b shows the FT spectra corresponding to Fig. 3a, where the leaky region is inside the grey circle. The FT spectrum contains large components inside the leaky region. As discussed, we consider

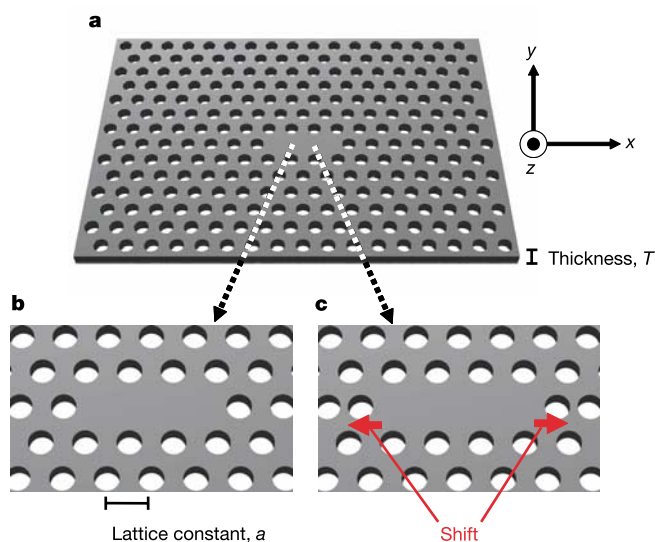


Figure 1 Photonic nanocavities using a 2D photonic-crystal slab. **a**, Schematic of the base cavity structure having a triangular lattice of air rods with lattice constant a ($= 0.42 \mu\text{m}$). The thickness T of the slab and the radius R of the air rods are $0.6a$ ($0.25 \mu\text{m}$) and $0.29a$ ($0.12 \mu\text{m}$), respectively. **b**, Starting cavity structure with three missing air rods in a line. **c**, Designed cavity structure created by displacing the air rods at both edges to obtain an ultrahigh Q/V value.

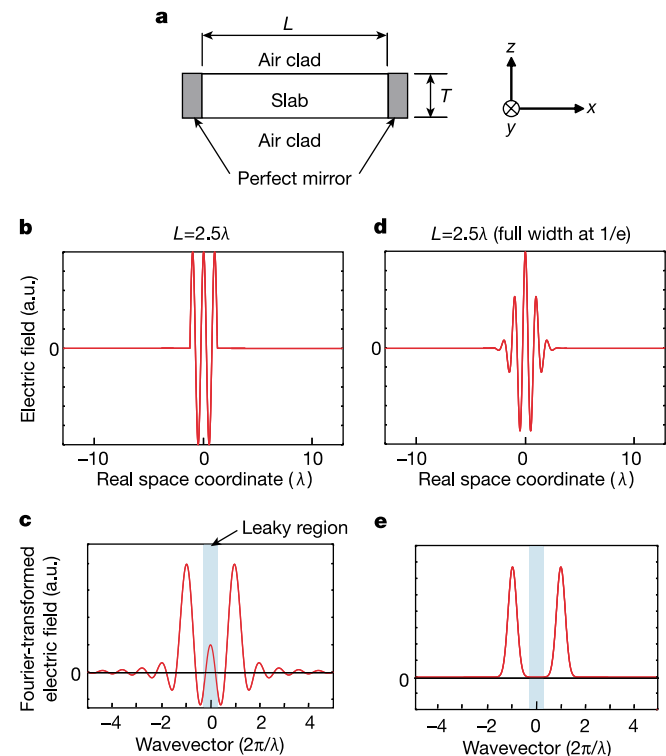


Figure 2 Analysis and reduction of cavity loss. **a**, Simplified model of a cavity consisting of a dielectric material with thickness T and length L . For confinement of light, both sides of the cavity are closed by perfect mirrors for the x direction, and by the air clad based on TIR for the z direction. **b**, **c**, The electric field profile inside a cavity with a very short (2.5λ) length, and the spatial FT spectra. The leaky region is indicated as a blue area. **d**, **e**, The electric field profile with a gentle envelope function (gaussian curve) and its spatial FT spectrum. a.u., arbitrary units.

that this is due to the abrupt change at the cavity edges. Here we try to make confinement gentler. The strategy to obtain gentler confinement is to change the condition for Bragg reflection at the cavity edge. Such reflection is determined by a summation of partial reflections at a series of rods near the cavity edge. When we move several rods near the cavity edge, the Bragg reflection condition should be modified. Because the phases of partial reflections at the moved rods are changed, the resultant phase-mismatch weakens the magnitude of Bragg reflection. To compensate for the reduction of the reflection, light is considered to penetrate more inside the mirror and be reflected perfectly. It means that the electric field profile at the cavity edge becomes gentler. With the appropriate movement of rods, the profile is considered to be close to the ideal confinement expressed by the gaussian function as discussed above. Using this strategy, the air rods at both edges of the cavity are shifted (Fig. 1c). Figure 3c and d show the electric field profile and 2D FT spectrum, respectively, where the shift of the air rods is $0.15a$ from their original position. As in Fig. 3d, the FT spectrum contains much smaller components inside the leaky region compared with Fig. 3b. The mode volume itself is confirmed as almost unchanged. Therefore, a significant increase of Q/V is expected to be achieved by this method.

Encouraged by the above analysis, we fabricated samples with various displacements. The resonant spectra were measured using a tunable c.w. laser as a light source. The cavities were excited through a line defect waveguide constructed by filling a row of air holes near the cavity (Fig. 4b), and the intensity of the light emitted from the cavities to free space was observed. Details of construction and experimental methods are given elsewhere¹⁷. The intrinsic Q factor of the cavity was determined from its radiation spectra by removing the effect of coupling between the cavity and the waveguide. The effective modal volume was calculated from the electric field profile of the cavity⁴; from this it was found that V is small and constant at $(6-7) \times 10^{-14} \text{ cm}^3$.

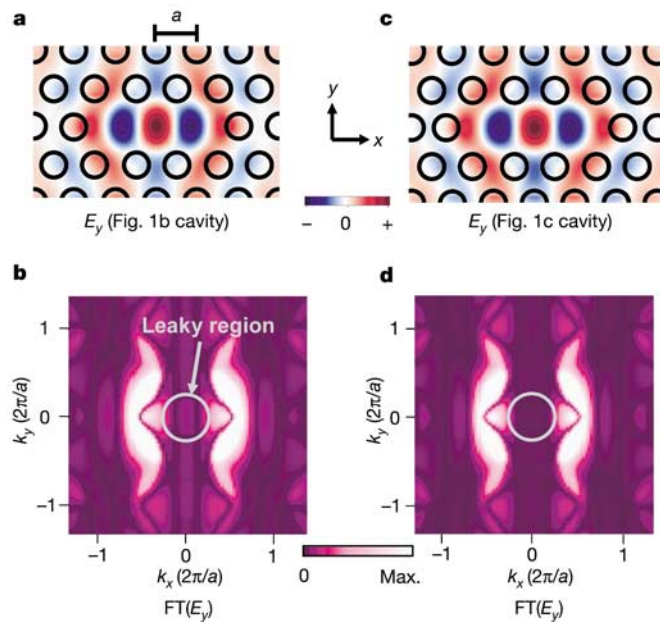


Figure 3 Physical design of high- Q/V cavity. **a**, The electric field profile (E_y) of the fundamental mode of the cavity shown in Fig. 1b as the starting structure. **b**, The FT spectra of **a**. The region inside the grey circle corresponds to the leaky region. **c**, **d**, The electric field profile and 2D FT spectrum, respectively, for the designed cavity shown in Fig. 1c. The displacement of the air rods at the edges is set at $0.15a$ from the starting structure shown in Fig. 1b.

Figures 4a and b show resonant spectra of cavities with various air-rod shifts and the corresponding scanning electron microscope (SEM) pictures, respectively. The width of the resonant peak changes drastically with shift of air rods. The spectral width becomes a minimum (0.045 nm) for the sample with shift $\sim 0.15a$, from which a Q factor of 45,000 is derived considering the coupling effect with the waveguide. In Fig. 4c, the Q/V values are plotted as a function of shift of air rods. Q/V increases by a factor of 10 upon increasing the air-rod shift up to $\sim 0.15a$. A Q/V as large as $6.4 \times 10^{17} \text{ cm}^{-3}$ or $120,000/\lambda^3$ has thus been obtained. This is one to two orders of magnitude higher than values for previously reported cavities such as toroid microcavities, microdisks and photonic-crystal cavities^{4,11-14}. Further increases of Q/V should be possible by fine-tuning the arrangement of air rods at the cavity edges to obtain the perfect gaussian curve for light confinement. The inset of Fig. 4a shows the spectrum measured for a wide wavelength range, indicating that no other resonant peak exists in the range 1,500 to 1,600 nm. The result shows that single-mode operation is possible for a broad range of wavelengths, which is very useful for various applications.

We have described the important design rule that light should be confined gently to obtain high Q factors while maintaining a very small modal volume V . An extremely large Q/V value has been achieved by introducing displacement of air rods at both edges of a cavity in a 2D photonic-crystal slab. We believe that this concept could be applied to the design of various types of photonic nanocavity; such high- Q nanocavities could be applied across various fields of science and engineering, including nano-lasers, nonlinear optics, nano-biomaterials, atom physics, and quantum computing. The present result is also important for the field of

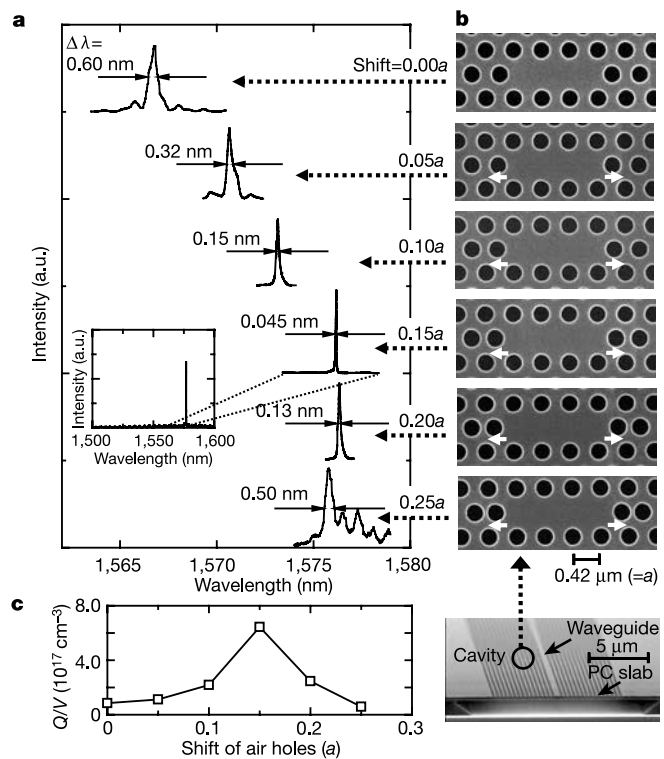


Figure 4 Experimental results. **a**, **b**, Resonant spectra of cavities with various shifts of air rods and their SEM pictures, respectively. PC, photonic crystal. The inset in **a** shows the resonant spectrum of the cavity (with $0.15a$ displacement) measured over a wide wavelength range. **c**, The estimated Q/V values as a function of shift of air rods. A maximum value of $Q/V = 6.4 \times 10^{17} \text{ cm}^{-3}$, or $120,000/\lambda^3$, has been realized.

photonic-crystal-based integrated circuits, as strong 3D confinement of photons in an ultra-small cavity has been realized, and leakage in the vertical direction sufficiently suppressed. □

Received 24 July; accepted 12 September 2003; doi:10.1038/nature02063.

1. Khitrova, G., Gibbs, H. M., Jahnke, F., Kira, M. & Koch, S. W. Nonlinear optics of normal-mode-coupling semiconductor microcavities. *Rev. Mod. Phys.* **71**, 1591–1639 (1999).
2. Noda, S., Chutinan, A. & Imada, M. Trapping and emission of photons by a single defect in a photonic bandgap structure. *Nature* **407**, 608–610 (2000).
3. Song, B. S., Noda, S. & Asano, T. Photonic devices based on in-plane hetero photonic crystals. *Science* **300**, 1537 (2003).
4. Painter, O. *et al.* Two-dimensional photonic band-gap defect mode laser. *Science* **284**, 1819–1821 (1999).
5. Noda, S., Tomoda, K., Yamamoto, N. & Chutinan, A. Full three-dimensional photonic bandgap crystals at near-infrared wavelengths. *Science* **289**, 604–606 (2000).
6. Spillane, S. M., Kippenberg, T. J. & Vahala, K. J. Ultralow-threshold Raman laser using a spherical dielectric microcavity. *Nature* **415**, 621–623 (2002).
7. Michler, P. *et al.* A quantum dot single-photon turnstile device. *Science* **290**, 2282–2285 (2000).
8. Johnson, S. G., Fan, S., Mekis, A. & Joannopoulos, J. D. Multipole-cancellation mechanism for high-Q cavities in the absence of a complete photonic band gap. *Appl. Phys. Lett.* **78**, 3388–3390 (2001).
9. Vučković, J., Lončar, M., Mabuchi, H. & Scherer, A. Design of photonic crystal microcavities for cavity QED. *Phys. Rev. E* **65**, 016608 (2001).
10. Srinivasan, K. & Painter, O. Momentum space design of high-Q photonic crystal optical cavities. *Opt. Express* **10**, 670–684 (2002).
11. Gayral, B. *et al.* High-Q wet-etched GaAs microdisks containing InAs quantum boxes. *Appl. Phys. Lett.* **75**, 1908–1910 (1999).
12. Yoshie, T., Vučković, J., Scherer, A., Chen, H. & Deppe, D. High quality two-dimensional photonic crystal slab cavities. *Appl. Phys. Lett.* **79**, 4289–4291 (2001).
13. Ryu, H. Y. *et al.* Square-lattice photonic band-gap single-cell laser operating in the lower-order whispering gallery mode. *Appl. Phys. Lett.* **80**, 3883–3885 (2002).
14. Armani, D. K., Kippenberg, T. J., Spillane, S. M. & Vahala, K. J. Ultra-high-Q toroid microcavity on a chip. *Nature* **421**, 925–928 (2003).
15. Vernooy, D. W., Ilchenko, V. S., Mabuchi, H., Streed, E. W. & Kimble, H. J. High-Q measurements of fused-silica microspheres in the near infrared. *Opt. Lett.* **23**, 247–249 (1998).
16. Yablonovitch, E. Inhibited spontaneous emission in solid-state physics and electronics. *Phys. Rev. Lett.* **58**, 2059–2062 (1987).
17. Akahane, Y., Asano, T., Song, B. S. & Noda, S. Investigation of high-Q channel drop filters using donor-type defects in two-dimensional photonic crystal slabs. *Appl. Phys. Lett.* **83**, 1512–1514 (2003).

Acknowledgements This work was supported partly by Grant-in-Aid from the Ministry of Education, Culture, Sports, Science and Technology of Japan, and also by CREST, Japan Science and Technology Corporation.

Competing interests statement The authors declare that they have no competing financial interests.

Correspondence and requests for materials should be addressed to S.N. (snoda@kuee.kyoto-u.ac.jp).

High interannual variability of sea ice thickness in the Arctic region

Seymour Laxon¹, Neil Peacock¹ & Doug Smith²

¹Centre for Polar Observation and Modelling, University College London, Gower Street, London WC1E 6BT, UK

²Met Office Hadley Centre for Climate Prediction and Research, FitzRoy Road, Exeter, Devon EX1 3PB, UK

Possible future changes in Arctic sea ice cover and thickness, and consequent changes in the ice-albedo feedback, represent one of the largest uncertainties in the prediction of future temperature rise^{1,2}. Knowledge of the natural variability of sea ice thickness is therefore critical for its representation in global climate models^{3,4}. Numerical simulations suggest that Arctic ice thickness varies primarily on decadal timescales^{3,5,6} owing to changes in wind and ocean stresses on the ice^{7–10}, but observations have been unable to provide a synoptic view of sea ice thickness, which is required to validate the model results^{3,6,9}. Here we use an eight-year time-series of Arctic ice thickness, derived from satellite

altimeter measurements of ice freeboard, to determine the mean thickness field and its variability from 65° N to 81.5° N. Our data reveal a high-frequency interannual variability in mean Arctic ice thickness that is dominated by changes in the amount of summer melt¹¹, rather than by changes in circulation. Our results suggest that a continued increase in melt season length would lead to further thinning of Arctic sea ice.

The prediction of future changes in Arctic sea ice, and consequent effects on the ocean¹² and atmosphere², relies on global climate models properly reproducing changes in ice thickness^{3,4,13}. Knowledge of ice thickness variability is also critical in determining whether observed changes¹⁴ are natural, or anthropogenic, in origin⁴. The sparseness of sea ice thickness observations means that current understanding of the regional, and interannual, variability of sea ice thickness is entirely based on numerical models of the Arctic^{6,9}. However, it is unclear from model results whether ice thickness is controlled mainly by changes in thermodynamic (radiative or thermal) forcing⁵, or by dynamic (ocean and wind stress) forcing⁷. The majority of Arctic Ocean models suggest that variability in Arctic ice thickness occurs on decadal timescales^{5,6,9}, and is caused mainly by dynamic forcing^{6–8}. Simulations of Arctic ice cover covering the past four decades have been used to argue that observed thin ice^{14–17} during the 1990s was a result of changes in atmospheric^{6,7,10,17} or oceanic^{8,18} circulation. However, numerical simulations of ice thickness are undermined by uncertainties in the representation of physical processes⁹, and by differences in methods used to couple the ice, ocean and atmosphere¹², resulting in significant discrepancies between model simulations of ice thickness evolution¹⁴. The lack of continuous large-scale thickness measurements means that conclusions drawn from numerical simulations regarding the variability of Arctic sea ice thickness, and the processes that control it, remain untested^{3,12}.

We use newly developed techniques to obtain ice thickness from satellite estimates of ice freeboard over the 8-yr period 1993–2001 (Fig. 1). The region of coverage (ROC) extends to 81.5° N, covering an average area of 3.08×10^6 km², or more than half of the permanent sea ice cover. The data cover the entire circumference of the Arctic Ocean, including the Beaufort, Chukchi, East Siberian, Kara, Laptev, Barents and Greenland seas. We use measurements from the 13.8-GHz radar altimeters carried on the ERS-1 and ERS-2 satellites. By analysing individual echoes, we distinguish those originating from consolidated first and multi-year ice floes from those due to leads, open water and new ice. Corrections for orbits, tides, and atmospheric delay are applied to the radar data to obtain the elevation of ice floes and open water or new ice¹⁹. The elevation of the ice above the water surface is then obtained by subtracting the sea surface elevation, determined from open water measurements.

To deduce the ice thickness from ice elevation, the source of the echoes scattered from snow-covered sea ice must be determined. Laboratory experiments show that, under dry cold snow conditions, a normal-incidence 13.4-GHz radar reflection from snow-covered sea ice originates at the snow–ice interface²⁰. The ERS radar altimeter measurements of ice elevation therefore provide the level of the snow–ice interface above the water level—that is, the ice freeboard. We convert the ice freeboard measurements to ice thickness by assuming hydrostatic equilibrium, and then using fixed densities of ice (915.1 kg m^{-3}) and sea water ($1,023.9 \text{ kg m}^{-3}$)²¹ and a monthly climatology of snow depth and density²². The estimated uncertainty in ice and water density, of $\pm 5 \text{ kg m}^{-3}$ and $\pm 0.5 \text{ kg m}^{-3}$ respectively²¹, results in an uncertainty of ± 11 cm for our mean thickness. Interannual variability in snow loading, estimated²³ to be between 2 and 3 cm, results in a further uncertainty of 6 to 9 cm in our ice thickness estimates. Figure 2 compares ERS thickness estimates with those derived from near-coincident submarine draught measurements¹⁵. A linear least-squares fit, weighted by the estimated measurement, snow loading and ice/water density uncertainties, shows that the correlation between the altimeter and